2014 5th IEEE RAS & EMBS International Conference on
Biomedical Robotics and Biomechatronics (BioRob)
August 12-15, 2014. São Paulo, Brazil

Relationship between workspace reduction due to collisions and distance between endoscope and target organ in pediatric endoscopic surgery

M. Fujii, *IEEE Student Member*, S. Takazawa, K. Harada, *IEEE Member*, N. Sugita, T. Ishimaru, T. Iwanaka, and M. Mitsuishi, *IEEE Member*

***Abstract*—We investigated the relationship between workspace reduction due to collisions and the distance between the endoscope and target organ to develop a new algorithm for endoscope navigation in pediatric endoscopic surgery. Proper endoscope position is important for pediatric endoscopic surgery: the endoscope needs to get close to the target organ to obtain a suitable field of view. However, collisions between the endoscope and instrument are more likely to happen when the endoscope get close to the target. This reduces the workspace and complicates pediatric endoscopic surgery. We developed a simplified model of the endoscope and instrument to simulate the influence of the distance between the endoscope and target on the workspace reduction due to collisions. The simulation results showed how the workspace reduction was affected. Based on the results, we will perform further experiments to determine the appropriate endoscope position.**

I. Introduction

Endoscopic surgery is widely performed in pediatric surgery. It has many advantages for patients such as early recovery, less pain, shorter hospital stays, and better cosmetic results. However, surgeons must possess more skill and experience than for open surgery because the instrument motion is restricted by the insertion point.

The endoscope position is also important in endoscopic surgery. An appropriate endoscope position creates a suitable field of view and results in a good surgical outcome. Otherwise, surgeons struggle with problems such as collision between the endoscope and instrument. Many studies on general endoscopic surgery have developed methods for endoscope navigation and ensuring good endoscope position. Baumhauer et al. developed image guided therapy with augmented reality for laparoscopy [1]. Omote et al. developed a self-guided robot for laparoscopic surgery [2]. Tamadazte et al. developed an enhanced vision system for laparoscopic surgery [3] where the endoscope is equipped with additional cameras to provide a wide view of the abdominal cavity. Weede et al. developed an endoscopic guidance system for minimally invasive surgery [4] that automatically tracks an instrument based on information extracted by trajectory clustering. Yu et al. developed an automatic visual window for a laparoscopic surgical robotic system [5]. Ortiz et al. developed a self-assistance endoscope robot [6]. Hanna et al. reported the influence of the direction of view, target-to-endoscope distance, and manipulation angle on endoscopic knot tying [7]; they used an endoscope with a 10 mm diameter and needle driver with a 5 mm diameter and concluded that a distance of 75–150 mm between the endoscope and target is suitable for intracorporeal knot tying. Surgeons often experience collisions between the endoscope and instruments when the distance between the endoscope and target is 50 mm.

These studies focused on general endoscopic surgery; however, applying their results to pediatric endoscopy seems difficult because of the specific problems of pediatric endoscopy. Pediatric endoscopic surgery is more difficult than general endoscopic surgery because of the small abdominal and thoracic cavities, so better surgical skills are required. Endoscope positioning is also more difficult for pediatric endoscopic surgery than general endoscopic surgery since the distance between the endoscope and target is often less than 50 mm because of the small abdominal and thoracic cavities.

Therefore, the ultimate goal of our research is to develop an endoscope navigation algorithm for pediatric endoscopic surgery. We are trying to realize a method of determining the appropriate endoscope position, which is free from collisions and creates suitable field of view. In this study, we investigated the relationship between the workspace reduction due to collisions and the distance between an endoscope and target as a first step towards realizing our objective. Knowing where workspace reduction occurs and the degree of workspace reduction is useful. For example, the location and time of collisions during suturing and ligaturing can be predicted, which allows the endoscope to be manipulated in cooperation with the instrument to avoid the collisions.

Section II details the simplified simulation model, consisting of an endoscope and instrument, and the collision detection method. Section III describes the simulation results, where two sets of parameters based on pediatric surgeons' opinions were used. Section IV discusses the simulation results. Finally, section V concludes the paper.

II. Materials and Method

A. Modeling

To determine the collisions between the instrument and endoscope, the instrument and endoscope shapes were modeled and described as shown in Fig. 1. A 3 mm diameter instrument and 5 mm diameter endoscope were modeled. In this research, 0° and 30° endoscopes were used. The

M. Fujii, K. Harada, N. Sugita, and M. Mitsuishi are with the Department of Mechanical Engineering, School of Engineering, The University of Tokyo, 113-8656 JAPAN email: fujii@nml.t.u-tokyo.ac.jp

S. Takazawa, T. Ishimaru, and T. Iwanaka are with Department of Pediatric Surgery, The University of Tokyo Hospital.

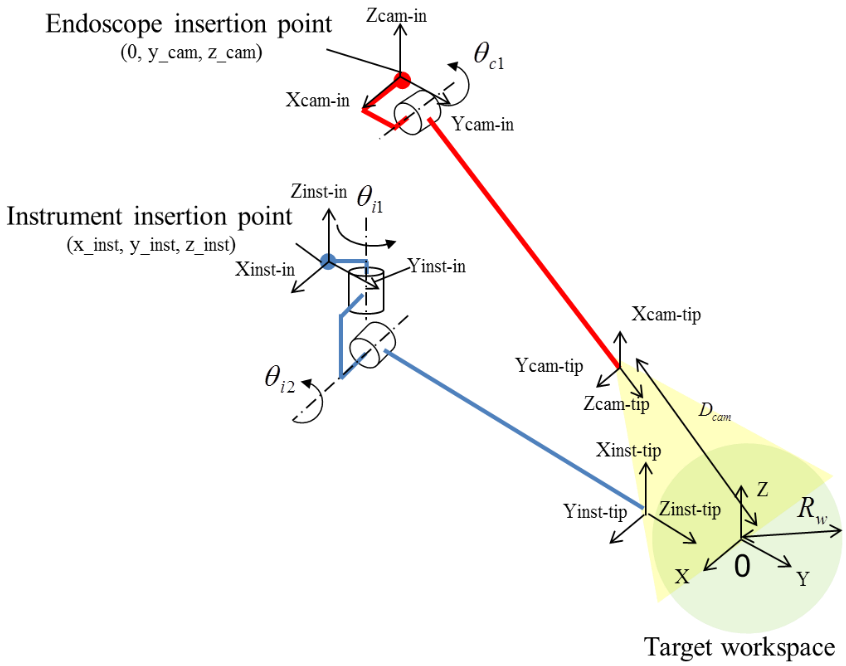

Figure 1. Simplified model of endoscope and instrument. The red line indicates the endoscope, and the blue line indicates the instrument. The yellow triangle indicates the field of view of the endoscope.

workspace was defined as a sphere with a radius of R_w, and frame {0} was fixed to the center of the target workspace. Frames {inst-in} and {cam-in} were fixed to the instrument and camera insertion points, respectively. Frames {inst-tip} and {camera-tip} were fixed to the instrument and camera tips, respectively. In frame {0}, the OZ axis was oriented upwards, and the OY axis was set so that the camera insertion point was on the OYZ plane to reduce the degrees of freedom of the endoscope. As shown in Fig. 1, ($x_{\_inst}$, $y_{\_inst}$, $z_{\_inst}$) and (0, $y_{\_cam}$, $z_{\_cam}$) were the coordinates of the instrument insertion point and endoscope insertion point, respectively, described in frame {0}. The orientation of the instrument was determined by θ_{i1} and θ_{i2}, and the orientation of the camera was determined by θ_{c1}. D_{cam} was the distance between the center of the target workspace and the endoscope tip.

B. Instrument Kinematics and Inverse Kinematics

Fig. 2 shows the endoscopic instrument kinematic diagram. The Denavit–Hartenberg (D-H) parameters in Table I were used to generate the elementary homogenous transformation matrix (HTM) of the instrument. Based on the D-H parameters in Table I and the coordinates of the instrument insertion point ($x_{\_inst}$, $y_{\_inst}$, $z_{\_inst}$), the HTM ($T_{0,inst-tip}$) is obtained as follows:

$$T_{0,inst-tip} = \begin{pmatrix} C_{i1}C_{i2} & S_{i1} & C_{i1}S_{i2} & R_{inst}C_{i1}S_{i2} + x_{\_inst} \\ S_{i1}C_{i2} & -C_{i1} & S_{i1}S_{i2} & R_{inst}S_{i1}S_{i2} + y_{\_inst} \\ S_{i2} & 0 & -C_{i2} & -R_{inst}C_{i2} + z_{\_inst} \\ 0 & 0 & 0 & 1 \end{pmatrix} \quad (1)$$

where S_{i1}, S_{i2}, C_{i1}, and C_{i2} indicate $\sin\theta_{i1}$, $\sin\theta_{i2}$, $\cos\theta_{i1}$, and $\cos\theta_{i2}$, respectively.

To determine the position of the instrument, the inverse kinematics has to be solved by an analytical method. The coordinates of the instrument tip ($x_{inst-tip}, y_{inst-tip}, z_{inst-tip}$) described in frame {0} are defined as follows:

$$x_{inst-tip}^2 + y_{inst-tip}^2 + z_{inst-tip}^2 \le R_w^2 \quad (2)$$

This is because the instrument tip moves in a spherical workspace. With (2), R_{inst}, θ_{i1}, and θ_{i2} are obtained as follows:

$$R_{inst} = \sqrt{(x_{inst-tip} - x_{\_inst})^2 + (y_{inst-tip} - y_{\_inst})^2 + (z_{inst-tip} - z_{\_inst})^2} \quad (3)$$

$$\theta_{i1} = \mathrm{atan}\,2(x_{\_inst} - x_{inst-tip}, y_{inst\_tip} - y_{\_inst}) \quad (4)$$

$$\theta_{i2} = \cos^{-1}\left(\frac{z_{\_inst} - z_{inst-tip}}{R_{inst}}\right) \quad (5)$$

Considering the diameter of the instrument, the coordinates of the instrument surface ($x_{inst\_surface}$, $y_{inst\_surface}$, $z_{inst\_surface}$) described in the frame {0} are obtained as follows:

$$\begin{pmatrix} x_{inst\_surface} \\ y_{inst\_surface} \\ z_{inst\_surface} \\ 1 \end{pmatrix} = T_{0,inst-tip} \begin{pmatrix} x_{inst-radius} \\ y_{inst-radius} \\ r_{inst-shaft} \\ 1 \end{pmatrix} \quad (6)$$

TABLE I. D-H PARAMETERS OF INSTRUMENT

Joint	Parameters			
	α_{i-1}	a_{i-1}	d_i	θ_i
inst-1	0	0	0	θ_{i1}
inst-2	$\frac{\pi}{2}$	0	0	θ_{i2}
inst-tip	$\frac{\pi}{2}$	0	R_{inst}	0

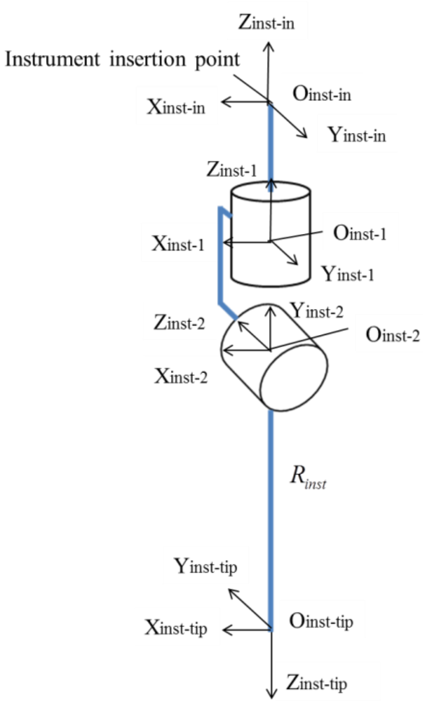

Figure 2. Kinematic diagram of instrument

where $x_{inst-radius}$ and $y_{inst-radius}$ indicate the boundary of the instrument shaft and $r_{inst-shaft}$ is the length from the instrument insertion point to the instrument tip. Therefore, (6) also fulfills the following equations:

$$x^2_{inst-radius} + y^2_{inst-radius} = r^2_{inst-radius} \qquad (7)$$

$$-R_{inst} \le r_{inst-shaft} \le 0 \qquad (8)$$

In (7), $r_{inst-radius}$ indicates the radius of the instrument.

C. *Endoscope Kinematics and Inverse Kinematics*

Fig. 3 shows the endoscope kinematic diagram. The D-H parameters in table II are used to generate the elementary HTM of the endoscope. Using the D-H parameters in Table II and the coordinates of the endoscope insertion point (0 , $y_{\_cam}$, $z_{\_cam}$), the HTM ($T_{0,cam-tip}$) is obtained as follows:

TABLE II. D-H PARAMETERS OF ENDOSCOPE

Joint	Parameters			
	α_{i-1}	a_{i-1}	d_i	θ_i
cam-1	0	0	0	$\frac{\pi}{2}$
cam-2	$\frac{\pi}{2}$	0	0	θ_{c2}
cam-tip	$\frac{\pi}{2}$	0	R_{cam}	0

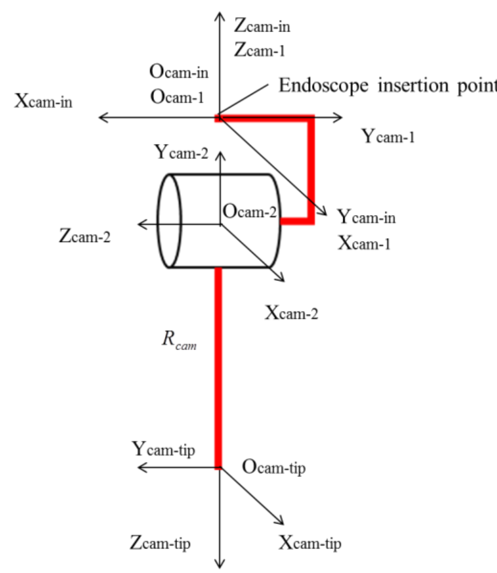

Figure 3. Kinematic diagram of endoscope

$$T_{0,cam-tip} = \begin{pmatrix} 0 & 1 & 0 & 0 \\ C_{c1} & 0 & S_{c1} & R_{cam}S_{c1} + y_{\_cam} \\ S_{c1} & 0 & -C_{c1} & -R_{cam}C_{c1} + z_{\_cam} \\ 0 & 0 & 0 & 1 \end{pmatrix} \qquad (9)$$

where S_{c2} and C_{c2} indicate $\sin\theta_{c2}$ and $\cos\theta_{c2}$, respectively.

To determine the position of the endoscope, the inverse kinematics has to be solved by an analytical method. θ_{c2} and R_{cam} are obtained as follows:

$$R_{cam}$$

$$= \sqrt{y^2_{\_cam} + z^2_{\_cam}}\cos(\sin^{-1}(\frac{D_{cam}\sin(\theta_{obl})}{\sqrt{y^2_{\_cam} + z^2_{\_cam}}})) - D_{cam}\cos(\theta_{obl}) \qquad (10)$$

$$\theta_{c1} = \tan^{-1}(\frac{-y_{\_cam}}{z_{\_cam}}) + \sin^{-1}(\frac{D_{cam}\sin(\theta_{obl})}{\sqrt{y^2_{\_cam} + z^2_{cam}}}) \qquad (11)$$

where D_{cam} and θ_{obl} are the distance between the center of the target workspace and the endoscope tip and the angle between the center of the visual field and the physical axis of the endoscope, respectively. Considering the diameter of the endoscope, the coordinates of the endoscope surface ($x_{end\_surface}$, $y_{end\_surface}$, $z_{end\_surface}$) described in the frame {0} are obtained as follows:

$$\begin{pmatrix} x_{end\_surface} \\ y_{end\_surface} \\ z_{end\_surface} \\ 1 \end{pmatrix} = T_{0,cam-tip} \begin{pmatrix} x_{cam-radius} \\ y_{cam-radius} \\ r_{cam-shaft} \\ 1 \end{pmatrix} \tag{12}$$

where $x_{cam-radius}$ and $y_{cam-radius}$ indicate the boundary of the endoscope shaft and $r_{cam-shaft}$ is the length from the endoscope insertion point to the endoscope tip. Therefore, (12) also fulfills the following equations:

$$x^2_{cam-radius} + y^2_{cam-radius} = r^2_{cam-radius} \tag{13}$$

$$-R_{cam} \le r_{cam-shaft} \le 0 \tag{14}$$

In (18), $r_{cam-radius}$ indicates the radius of the endoscope.

D. Collision Detection and Work Space Evaluation

The instrument shape expressed by the frame {0} coordinate needs to be converted to the frame {camera-tip} coordinate to detect collisions between the instrument and endoscope. With (6) and (12), the converted instrument shape is obtained as follows:

$$\begin{pmatrix} x_{inst-cam-tip} \\ y_{inst-cam-tip} \\ z_{ins-cam-tip} \\ 1 \end{pmatrix} = T^{-1}_{0,cam-tip} \cdot T_{0,inst-tip} \begin{pmatrix} x_{inst-radius} \\ y_{inst-radius} \\ r_{inst-shaft} \\ 1 \end{pmatrix} \tag{15}$$

where $x_{inst-cam-tip}$, $y_{inst-cam-tip}$, and $z_{inst-cam-tip}$ indicate the x coordinate of the instrument shape expressed by the frame {camera-tip}, the y coordinate of the instrument shape expressed by the frame {camera-tip}, and the z coordinate of the instrument shape expressed by the frame {camera-tip}, respectively. This equation also fulfills (7) and (8). If a collision occurs between the instrument and endoscope, $x_{inst-cam-tip}$, $y_{inst-cam-tip}$, and $z_{inst-cam-tip}$ fulfill both of the following equations:

$$x^2_{inst-cam-tip} + y^2_{inst-cam-tip} \le r^2_{cam-radius} \tag{16}$$

$$-R_{cam} \le z_{inst-cam-tip} \le 0 \tag{17}$$

This calculation with (3)–(5), (10), and (11) is performed by using all coordinates of the instrument tip ($x_{inst-tip}, y_{inst-tip}, z_{inst-tip}$) that fulfill (2). Based on the endoscope and instrument used in this simulation, $r_{cam-radius}$ and $r_{inst-radius}$ were represented by the values of 2.5 and 1.5, respectively. θ_{obl} was represented by the values of 0° or 30° because forward-viewing and 30° endoscopes were used in this simulation. Based on the results of the collision calculation, the workspace shape and volume were evaluated.

E. Simulation Setup

Based on the opinions of pediatric surgeons, two sets of parameters based on pediatric diseases were used for the simulation, as shown in table III: a model of congenital duodenal atresia [8] and a model of congenital esophageal atresia (c) [9]. These two were chosen because they require major laparoscopic and thoracoscopic neonatal surgery, and collisions often occur during surgery. In both models, the radius of the target workspace (R_w) was 15 mm considering the small abdominal and thoracic cavities of the pediatric patient. The distance between the endoscope tip and center of the target workspace (D_{cam}) was defined as a variable. The endoscope needed to get close to the target organ to create a clear field of view. On the other hand, when D_{cam} became short, collisions between the instrument and endoscope tended to occur. Therefore, D_{cam} was chosen as a variable. MATLAB was used to calculate the workspace volume.

TABLE III. SIMULATION PARAMETERS

Parameter	Congenital duodenal atresia	Congenital esophageal atresia (C)
L_{inst} (mm)	34.5	0
H_{inst} (mm)	30	42
W_{inst} (mm)	25	16
L_{cam} (mm)	34.5	7.5
H_{cam} (mm)	30	42
D_{cam} (mm)	30, 28, 26, 24, 22, 20	

III. RESULTS

Figs. 4 and 5 show the results of the congenital duodenal atresia and congenital esophageal atresia (c) models, respectively. As shown in Fig. 4, the workspace reduction in the congenital duodenal model with both forward-viewing and 30° endoscopes occurred when D_{cam} was 24 mm. The workspace reduction was larger when D_{cam} became shorter. The workspace reduction with the 30° endoscope differed from that with the forward-viewing endoscope. The former only occurred in the upper part of the target workspace, whereas the latter occurred in the middle part of the target workspace. As shown in Fig. 5, the workspace reduction in the congenital esophageal atresia (c) model with forward-viewing and 30° endoscopes occurred when D_{cam} were 26 and 28 mm, respectively. In this case, the workspace reduction was also larger when D_{cam} became shorter, and the workspace reduction volume with the 30° endoscope was larger than that with the forward-viewing endoscope. The workspace reduction with the 30° endoscope only occurred

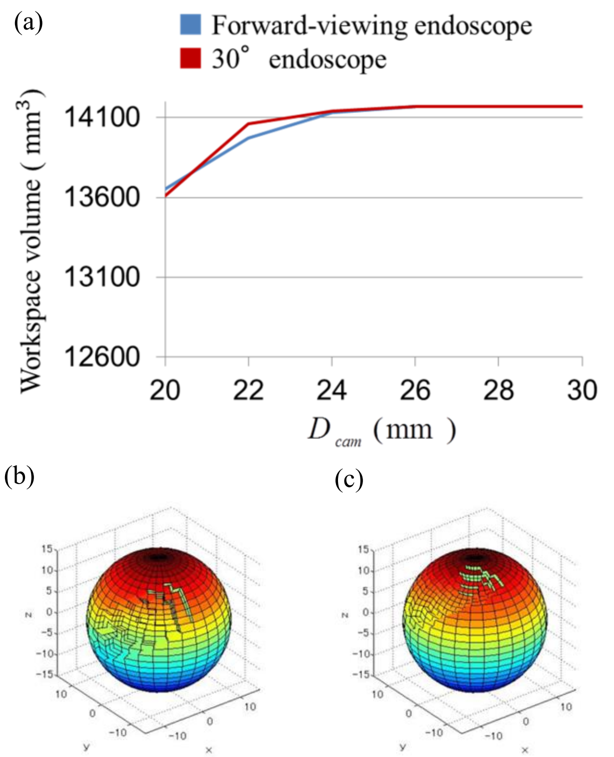

Figure 4. Simulation result of congenital duodenal atresia model: (a) relationship between D_{cam} and workspace volume, (b) shape of workspace with forward-viewing endoscope when D_{cam} is 20 mm, (c) shape of workspace with 30° endoscope when D_{cam} is 20 mm.

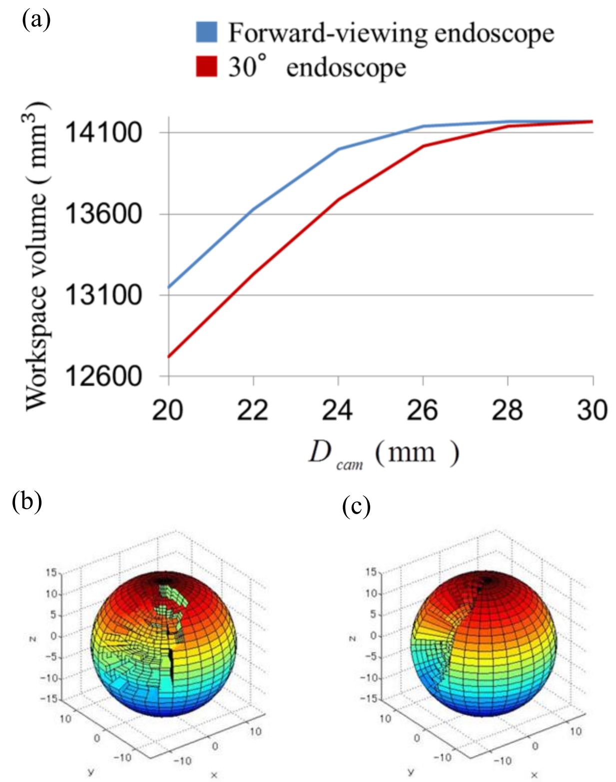

Figure 5. Simulation result of congenital esophageal atresia model: (a) relationship between D_{cam} and workspace volume, (b) shape of workspace with forward-viewing endoscope when D_{cam} is 20 mm, (c) shape of workspace with 30° endoscope when D_{cam} is 20 mm.

in the positive direction of the Y-axis shown in Fig. 5(c), whereas that with forward-viewing occurred in the negative direction of the Y-axis shown in Fig. 5(b). The shape of the workspace reduction in the congenital esophageal atresia (c) model differed from that of in the congenital duodenal atresia model. The reduction volume of the target workspace in the congenital esophageal atresia model (c) was also larger than that of the congenital duodenal atresia model.

IV. Discussion

The endoscope must create a suitable field of view for sutures in surgery on both congenital duodenal atresia (c) and congenital esophageal atresia. For congenital esophageal atresia (c), pediatric surgeons should perform anastomosis on the proximal esophagus, which is 10 mm in diameter, and the distal esophagus, which is 5 mm in diameter. For congenital duodenal atresia, a standard diamond anastomosis is performed after proximal and distal duodenotomies are made. The length of the incision part for diamond anastomosis is 10–15 mm. In both operations, the interval length of the suture should be less than 2 mm to prevent leakage from the anastomotic site. Therefore, both anastomoses need enlarged images of the target workspace for precise sutures. The simulation results indicated that the workspace volume decreased when the endoscope became close to the target. Therefore, we have to determine the endoscope position that creates the precise image of the target organs and maximizes the workspace volume.

The simulation results of the congenital esophageal atresia model showed that the workspace with the forward-viewing endoscope was larger than that with the 30° endoscope. Pediatric surgeons, however, prefer to use 30° endoscopes for congenital esophageal atresia because the target is hidden by the instrument when the forward-viewing endoscope is used. To develop an endoscope navigation algorithm for pediatric endoscopic surgery, an endoscope position that avoids the instrument hiding the target is also important.

The simulation result also implied that D_{cam} of the workspace volume reduction depends on the target disease and port placement. Only two sets of parameters based on pediatric diseases were used in this simulation. We must perform further simulations with different sets of parameters that are based on other diseases.

These simulation results are limited because instrument manipulation by the left hand, view obstruction by the instrument, the endoscope rotation, and one of the degrees of freedom of the endoscope were not considered. In this simulation, we focused on instrument manipulation by the right hand because it has the main role when driving a needle. To avoid collision between the endoscope and right-handed instrument and obstruction of the view by the instrument, the endoscope was moved in the negative direction of the X-axis of frame {0} in Fig. 1 while maintaining the length of D_{cam} because an oblique endoscope was used. However, assuming that the right- and left-handed instruments are inserted symmetrically to the YZ plane of frame {0}, the workspace reduction of the left-handed instrument will increase if the endoscope moves in such a direction. The obstruction of view by the left instrument will also increase. Cooperation between the right and left instruments is important for adjusting the needle holding point and ligaturing. Therefore, simulations that consider the left instrument, obstruction of view by both instruments, and an endoscope with four degree of freedoms (roll, pitch, yaw, and translation) should also be performed.

V. Conclusion

We performed simulations to demonstrate how collisions between two kinds of endoscopes and instrument reduce the workspace in pediatric endoscopic surgery. Based on the results, we will perform further experiments to determine the suitable endoscope position in pediatric endoscopic surgery to avoid collisions between the right and left instruments and the endoscope while maintaining a suitable field of view.

Acknowledgement

This research was supported by a Grant-in-Aid for a JSPS Fellow (247286)

References

[1] M. Baumhauer, et al. “The MITK image guided therapy toolkit and its application for augmented reality in laparoscopic prostate surgery,” SPIE Medical Imaging, pp. 76251G–76251G–7, 2010

[2] K. Omote, et al. “Self-guided robotic camera control for laparoscopic surgery compared with human camera control,” Am J Surg, vol. 177, no. 4, pp. 321-324,1999.

[3] B. Tamadazte, et al. “Enhanced vision system for laparoscopic surgery,” Conf. Proc. IEEE Eng. Med. Biol. Soc., vol. 2013, pp. 5702–5705, 2013.

[4] O. Weede, et al. “An intelligent and autonomous endoscopic guidance system for minimally invasive surgery,” 2011 IEEE Int. Conf. Robot. Autom., pp. 5762–5768, 2011.

[5] L. Yu, et al., “A kinematics method of automatic visual window for laparoscopic minimally invasive surgical robotic system,” 2013 IEEE Int. Conf. Mechatronics Autom., pp. 997–1002, 2013.

[6] S. Ortiz, et al. “Kinematic fundamentals of a biomechatronic laparoscopy system,” Int. J. Med. Robot. and Comput. Assist. Surg., vol. 7, no. 3, pp. 276–281, 2011.

[7] G. B. Hanna, et al. “Influence of direction of view, target-to-endoscope distance and manipulation angle on endoscopic knot tying.,” Br. J. Surg., vol. 84, no. 10, pp. 1460–1464, 1997.

[8] S. S. Rothenberg, “Laparoscopic Duodenoduodenostomy for Duodenal Obstruction in Infants and Children,” Journal of Pediatric Surgery, vol. 37, pp. 1088-1089, 2002.

[9] S. S. Rothenberg, “Thoracoscopic repair of esophageal atresia and trachea-esophageal fistula,” Seminars in Pediatric Surgery, vol. 14, pp. 2-7, 2005.